JOURNAL OF COMPUTATIONAL PHYSICS 15, 449–475 (1974)

Discrete Particle Effects in Whistler Simulation

J. DENAVIT

Department of Mechanical Engineering and Astronautical Sciences, Northwestern University, Evanston, Illinois, 60201

Received October 11, 1973

A particle code was written using weighted particles and a quiet start technique to simulate the nonlinear propagation of whistler waves parallel to an external magnetic field. The algorithm is derived from the Darwin Lagrangian by a variational method and two versions of the code are considered, using linear and quadratic splines. Numerical effects due to the discrete initial loading of the particles in parallel velocities, perpendicular velocity phase angles and positions are analyzed; and the performance of the linear and quadratic versions of the code are compared.

1. INTRODUCTION

This paper presents a particle simulation code primarily designed to simulate the nonlinear propagation of whistler waves parallel to an external magnetic field $\mathbf{B}_0$ in an electron plasma with a stationary positive neutralizing background. This code has recently been applied to numerical studies related to the theory of triggered Very-Low-Frequency (VLF) radio emissions from the Magnetosphere [1], and is applicable to loss-cone diffusion effects in controlled thermonuclear fusion devices. In particular it has been used to simulate the "antenna effect" in the propagation of whistler wavepackets and to investigate a plasma instability due to phase correlation of the electron perpendicular velocities [2]. These applications will be published elsewhere and the present paper is devoted to a description of the algorithm and a study of numerical effects due to the discrete nature of the particle and field representations.

The whistler mode corresponds to plasma waves propagating in the direction of an externally applied magnetic field $\mathbf{B}_0$ with circularly polarized wave fields. In the problems considered in this paper propagation parallel to $\mathbf{B}_0$ will be assumed. The wave vector potential $\mathbf{A}$ in this case is perpendicular to $\mathbf{B}_0$ and at any given time the tips of the local $\mathbf{A}$ vectors form a helix as shown in Fig. 1a. The dispersion relation for the whistler mode is

$$1 + \frac{\omega_p^2}{k^2c^2}\int\left[\frac{\omega - kv_x}{\omega - kv_x - \omega_c} + \frac{1}{2}\frac{k^2v_\perp^2}{(\omega - kv_x - \omega_c)^2}\right] f(v_x, v_\perp)\, d\mathbf{v} = 0. \qquad (1)$$

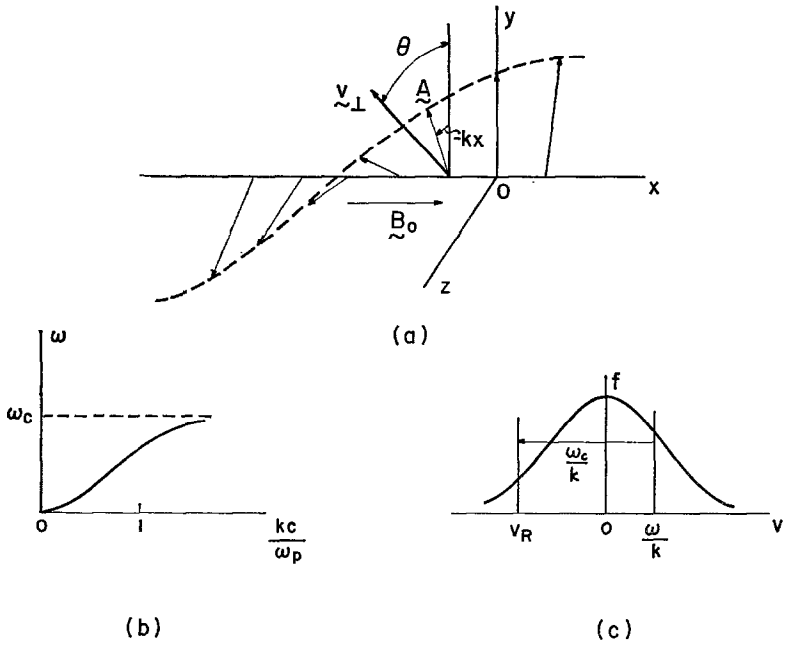

FIG. 1. (a) Geometric definition of a whistler wave showing the external magnetic field $\mathbf{B}_0$, the wave vector potential $\mathbf{A}$ and a typical electron perpendicular velocity $\mathbf{v}_\perp$. (b) Dispersion curve. (c) Parallel velocity distribution function showing the phase velocity ω/k and the resonant velocity v_R.

Here $\mathbf{v}_x$ and $\mathbf{v}_\perp$ are the electron velocities respectively parallel and perpendicular to $\mathbf{B}_0$, ω is the frequency, k is the wavenumber, $\omega_c = eB_0/mc$ is the electron cyclotron frequency, $\omega_p = (4\pi e^2 n_0/m)^{1/2}$ is the plasma frequency, n_0 is the electron density, $-e$ and m are the electron charge and mass and c is the speed of light [3]. This dispersion relation shows that the whistler frequency ω is smaller than the cyclotron frequency, Fig. 1b, and that a resonance exists for electrons having a parallel velocity near $v_R = (\omega - \omega_c)/k$, Fig. 1c. Resonant electrons travel in opposite direction from the wave and as they gyrate with angular velocity ω_c, their perpendicular velocity remains in phase with the local wave vector potential, causing them to interact strongly with the wave. This results in the cyclotron damping or amplification of the wave. In the case of a large-amplitude wave, resonant electrons can become trapped in the sense that the phase angle ζ of their perpendicular velocity relative to the local vector potential oscillates at the trapping frequency $\omega_T = k(eAv_\perp/mc)^{1/2}$ [4].

Note that the integral in Eq. (1) can be integrated with respect to $\mathbf{v}_\perp$ to give a dispersion relation which depends only on the moments $\eta_1(v_x) = \int v_\perp f\, dv_\perp$ and

$\eta_2(v_x) = \int v_\perp^3 f \, dv_\perp$ of f with respect to $v_\perp$. Thus the linear behavior of the plasma is not altered by assuming an electron distribution which is monoenergetic in the perpendicular direction for each value of the parallel velocity, i.e.,

$$f(v_x, v_\perp) = f_0(v_x)\, \delta[v_\perp - v_{\perp 0}(v_x)],$$

provided that the moments $\eta_1(v_x)$ and $\eta_2(v_x)$ are unchanged. Proper choice of the two functions $f_0(x_x)$ and $v_{\perp 0}(v_x)$ can reproduce both moments $\eta_1(v_x)$ and $\eta_2(v_x)$ independently, including for example the moments of a loss-cone distribution for which the ratio $\eta_2(v_x)/\eta_1(v_x) = v_{\perp 0}^2(v_x)$ is a function of v_x. This simplification allows the study of a number of problems with particles distributed around a single circle in the v_y, v_z plane for each value of v_x, and limits the need for a full distribution of particles to the study of effects due to energy spread in the perpendicular direction.

The present code is one-dimensional with spatial variation along the external magnetic field only (x direction) and periodic boundary conditions with periodicity length L. Only the motions of electrons are considered and the ions are replaced by a uniform positive charge distribution. The phase space is four-dimensional with position x and three velocities v_x, v_y and v_z. In order to study low-amplitude phenomena, a quiet start method is used with a regular initial loading of the simulation particles in phase space. For this purpose, the x, v_x plane is covered with a grid with mesh sizes Δx and Δv_x, Fig. 2a, and a set of weighted simulation particles is loaded at each grid point (x, v_x). Each set consists of particles with perpendicular velocities distributed at regular angular intervals $\Delta\theta$ around concentric circles in the v_y, v_z plane as shown in Fig. 2b. The charge over mass ratio is

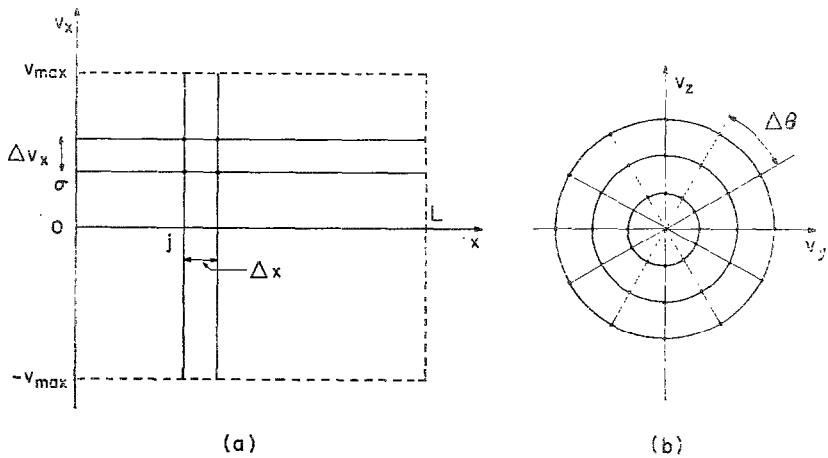

FIG. 2. Grid structure defining the discrete loading of particles in phase space.

$-e/m$ for all simulation particles, but the mass (and charge) of the simulation particles are chosen proportional to the local value of the initial distribution function in phase space. This regular loading of weighted particles avoids the undesirable initial fluctuations present in the more conventional random loading techniques, but it is responsible for numerical effects which excite nonphysical perturbations. The simulation of low-amplitude phenomena over a reasonable time therefore requires an understanding of these anomalous excitations and the selection of the proper algorithm and numerical parameters to minimize their effect.

The algorithm used to compute the self fields and to advance the particles is described in Section 2. Two versions of the algorithm are considered using linear and quadratic spline interpolations of the potentials. The numerical effects due to discrete loading of the particles are considered in the next three Sections. The first effect, to be considered in Section 3, is the whistler-mode beaming instability resulting from the interaction of discrete sets of beams with a finite velocity separation Δv_x. The second effect is due to the discrete distribution in the angular phase θ of the perpendicular velocities of the particles, which causes an excitation of electrostatic modes. This effect is discussed in Section 4. A third type of nonphysical perturbations results from the finite grid spacing Δx. The discrete representation of potentials yields whistler-mode aliases [5]. In addition, the regular loading of particles at grid points causes an excitation of oscillations with frequencies $\omega_0 + 2\pi\sigma\Delta v_x/\Delta x$ where ω_0 is the main wave frequency and σ is an integer. This effect is considered in Section V. The three types of numerical effects have been observed in numerical simulations and the results of a comparative study of these effects, using the linear and quadratic versions of the code, are included.

2. Algorithm

A. *Finite-Difference Equations*

Since whistler waves propagate at low frequency, in the range 200–30,000 Hz for magnetosphere whistlers for example, it is possible to neglect radiation in the self-field computations and the algorithm is derived from the Darwin Lagrangian [6, 7],

$$\mathscr{L} = \int_0^L \frac{E_x^2 - B^2}{8\pi}\, dx - \sum_{i=1}^{N} q_i \left[\Phi(x_i) - \frac{\mathbf{v}_i \cdot \mathbf{A}(x_i)}{c}\right]$$

$$- \int_0^L \rho_0 \Phi(x)\, dx + \frac{1}{2}\sum_{i=1}^{N} m_i v_i^2. \tag{2}$$

Here $\Phi(x)$ and $\mathbf{A}(x)$ are the scalar and vector potentials, ρ_0 is the uniform ion charge density, $\mathbf{B} = \nabla \times \mathbf{A}$ is the magnetic field, q_i, m_i, x_i and $\mathbf{v}_i$ denote the charge, mass, position and velocity of the N simulation particles. Note that in the first term only the Coulomb field $\mathbf{E}_x = -\nabla\Phi$ is included in the electric field energy. This is a distinctive feature of the Darwin Lagrangian, which results in the absence of retardation terms in the resulting field equations. The resulting model retains induced electric and magnetic fields, as well as the Coulomb field, but no radiation.

The finite-difference equations for the fields are obtained by the variational method of H. R. Lewis [8] by expanding the internal (or wave) potentials in the form

$$\Phi(x, t) = \sum_{j=1}^{J} \alpha_j(t)\, \varphi(x - j\Delta x) \tag{3}$$

and

$$\mathbf{A}(x, t) = \sum_{j=1}^{J} \beta_j(t)\, \varphi(x - j\Delta x) \tag{4}$$

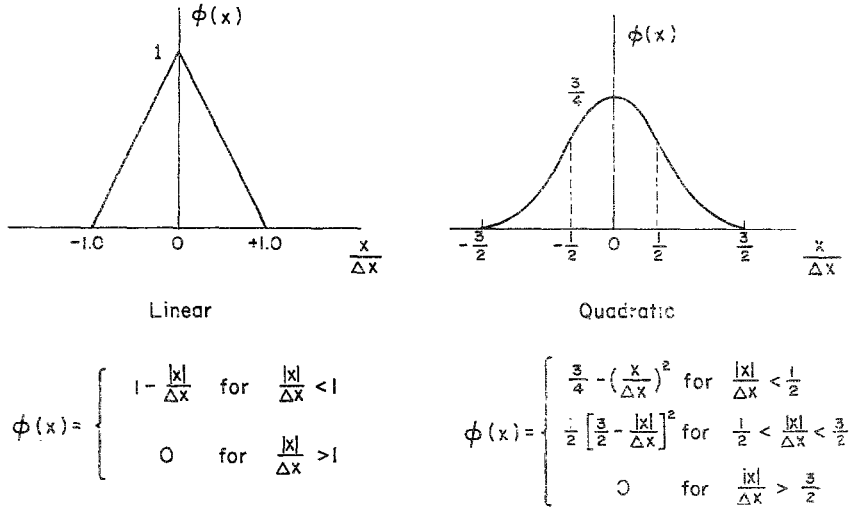

FIG. 3. Linear and quadratic splines.

where the basis function $\varphi(x)$ also known as the spline determines the interpolation used to define values of Φ and $\mathbf{A}$ for arbitrary values of x. Both linear and quadratic splines, defined in Fig. 3, are considered. Substituting these expansions into the Lagrangian and observing that the vector potential is perpendicular to the direction of propagation yields

$$\mathscr{L} = \frac{1}{8\pi}\int_0^L \left\{\left[\sum_{j=1}^{J}\alpha_j\varphi_j'\right]^2 - \left[\sum_{j=1}^{J}\beta_{yj}\varphi_j\right]^2 - \left[\sum_{j=1}^{J}\beta_{zj}\varphi_j'\right]^2\right\} dx$$

$$- \int_0^L \rho_0 \sum_{j=1}^{J}\alpha_j\varphi_j\, dx + \sum_{i=1}^{N} q_i \sum_{j=1}^{J}\left(-\alpha_j + \frac{1}{c}\dot{y}_i\beta_{yj} + \frac{1}{c}\dot{z}_i\beta_{zj}\right)\varphi_j$$

$$+ \frac{1}{2}\sum_{i=1}^{N} m_i(\dot{x}_i^2 + \dot{y}_i^2 + \dot{z}_i^2), \tag{5}$$

where the dot denotes time differentiation,

$$\varphi_j = \varphi(x - j\Delta x) \qquad \text{and} \qquad \varphi_j' = d\varphi(x - j\Delta x)/dx.$$

The equations for the particle dynamics are obtained by writing the Euler–Lagrange equations corresponding to the generalized coordinates x_i, y_i, z_i with $i = 1,..., N$ and adding the Lorentz force due to the external field **B** which is not included in the Lagrangian [9]. These operations yield

$$\frac{dv_{xi}}{dt} = \frac{q_i}{m_i}\sum_{j=1}^{J}\left(-\alpha_j + \frac{1}{c}v_{yi}\beta_{yj} + \frac{1}{c}v_{zi}\beta_{zj}\right)\varphi'(x_i - j\Delta x), \tag{6}$$

and

$$\frac{d}{dt}\left[m_i\mathbf{v}_{\perp i} + \frac{q_i}{c}\sum_{j=1}^{J}\boldsymbol{\beta}_j\varphi(x_i - j\Delta x)\right] = \frac{q_i}{c}(\mathbf{v}_{\perp i}\times\mathbf{B}_0) \tag{7}$$

where the bracket in the left member of Eq. (7) is recognized as the perpendicular canonical momentum of particle i in the internal potential **A**. Particular forms taken by these equations in the case of linear and quadratic splines are given in Appendix A.

The field equations are obtained by writing the Euler–Lagrange equations for the generalized coordinates α_j, β_{jy} and β_{jz} with $j = 1,..., J$,

$$\sum_{j'=1}^{J}\alpha_{j'}\int_0^L \varphi_{j'}'\varphi_j'\, dx = 4\pi\rho_0\int_0^L \varphi_j\, dx + 4\pi\sum_{i=1}^{N} q_i\varphi(x_i - j\Delta x) \tag{8}$$

and

$$\sum_{j'=1}^{J}\beta_{j'}\int_0^L \varphi_{j'}'\varphi_j'\, dx = \frac{4\pi}{c}\sum_{i=1}^{N} q_i\mathbf{v}_{\perp i}\varphi(x_i - j\Delta x). \tag{9}$$

The first of these equations is recognized as Poisson's equation and the second as Ampère's law written in terms of the vector potential. The integral $\int \varphi_{j'}'\,\varphi_j'\, dx$ is the appropriate form of the second derivative operator corresponding to the spline

$\varphi(x)$ and the spline also defines the charge sharing scheme to compute the charge and current densities in the right members of Eqs. (8) and (9). The particular forms taken by the derivative operator and charge sharing scheme for linear and quadratic splines are given in Appendix A.

B. *Time Step*

The particles and fields are advanced in time following a method based on perpendicular canonical momenta which has been used in previous codes using the Darwin model [10]. The particle positions x_i and perpendicular velocities $\mathbf{v}_{\perp i}$, as well as the potentials α_j and β_j, are computed at times $n\Delta t$ and the parallel velocities v_{xi} are computed at half time steps $(n - 1/2)\,\Delta t$ as shown in Fig. 4. It will be

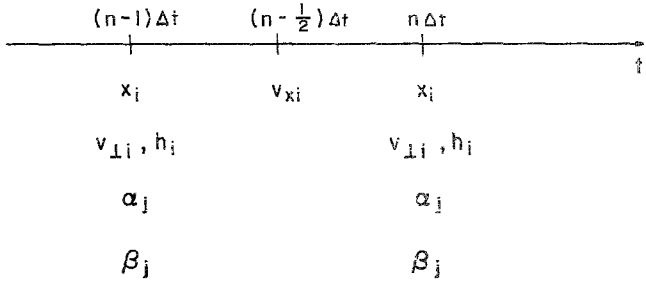

FIG. 4. Time step.

convenient to denote vectors perpendicular to the direction of propagation in complex number form with their y component represented by the real part and their z component represented by the imaginary part. With this notaion Eq. (7) takes the form

$$\frac{d}{dt}\left(v_{\perp i} + \frac{q_i}{m_i c} A_{\perp i}\right) = i\omega_c v_{\perp i} \tag{10}$$

where

$$A_{\perp i} = \sum_{j=1}^{J} \beta_j \varphi(x_i - j\Delta x) \tag{10a}$$

and we observe that the ratio $q_i/m_i = -e/m$ is the same for all simulation particles. To second order in Δt, Eq. (10) yields

$$(1 - i\delta_c)\, v_{\perp i}^n + (q_i/m_i c)\, A_{\perp i}^n = (1 + i\delta_c)\, v_{\perp i}^{n-1} + (q_i/m_i c)\, A_{\perp i}^{n-1} \tag{11}$$

where $\delta_c = \omega_c \Delta t/2$ and the superscripts denote time values. Let

$$h_i^n = (1 - i\delta_c)\, v_{\perp i}^n + (q_i/m_i c)\, A_{\perp i}^n$$

denote a modified form of the perpendicular canonical momentum of particle i at time $n\Delta t$, then Eq. (11) yields

$$h_i^n = \frac{q_i}{m_i c} \frac{2i\delta_c}{1 + i\delta_c} A_{\perp i}^n + \frac{1 - i\delta_c}{1 + i\delta_c} h_i^{n-1} \tag{12}$$

and

$$v_{\perp i}^n = \frac{1}{1 + i\delta_c} \left(h_i^{n-1} - \frac{q_i}{m_i c} A_{\perp i}^n \right). \tag{12a}$$

Let us assume that the computation has proceeded to the point where all quantities are known up to and including time $(n - 1)\,\Delta t$. A leap frog step applied to Eq. (6) yields $v_{xi}^{n-1/2}$ and x_i^n. The charge density may then be computed at time $n\Delta t$ and Eq. (8) yields the scalar potentials α_j^n as in electrostatic computations [11]. Since the computation of either h_i^n or $v_{\perp i}^n$ from Eqs. (12) or (12a) requires knowledge of $A_{\perp i}^n$, the vector potentials β_j^n at the new time $n\Delta t$ must be computed first. This is achieved by substituting Eq. (12a) into Eq. (9) to eliminate $v_{\perp i}^n$ and rearranging terms to obtain an equation for β_j^n in terms of known quantities,

$$\sum_{j'=1}^{J} \left[\int_0^L \varphi_{j'}' \varphi_{j}'\, dx + \frac{4\pi q_i}{m_i c^2} \frac{1}{1 + i\delta_c} \sum_{i=1}^{N} q_i \varphi(x_i^n - j\Delta x)\, \varphi(x_i^n - j'\Delta x) \right] \beta_{j'}$$
$$= \frac{4\pi}{c} \frac{1}{1 + i\delta_c} \sum_{i=1}^{N} q_i h_i^{n-1} \varphi(x_i^n - j\Delta x). \tag{13}$$

In the case of the linear spline, the operator $\int_0^L \varphi_{j'}'\, \varphi_j'\, dx$ takes the standard form

$$\int_0^L \varphi'(x - j'\Delta x)\, \varphi'(x - j\Delta)\, dx = \begin{cases} 2/\Delta x & \text{for } j' - j = 0, \\ -1/\Delta x & \text{for } |j' - j| = 1, \\ 0 & \text{for } |j' - j| > 1, \end{cases} \tag{14}$$

and the second term in bracket in the left member of Eq. (13) is nonzero only for $|j' - j| \leqslant 1$. In this case the left member of Eq. (13) therefore reduces to three terms.

$$A_j \beta_{j-1} + B_j \beta_j + C_j \beta_{j+1} = D_j \tag{13a}$$

where the quantities A_j, B_j, C_j and D_j, which depend on known charge and momentum distributions, are defined in Appendix A. Writing Eq. (13a) with $j = 1,..., J$ and applying periodic boundary conditions yields a system of equations having a tridiagonal coefficient matrix with nonzero off-diagonal corner elements,

$$\begin{aligned}
B_1\beta_1 + C_1\beta_2 \qquad\qquad\qquad\qquad + A_1\beta_J &= D_1, \\
A_2\beta_1 + B_2\beta_2 + C_2\beta_3 \qquad\qquad\quad &= D_2, \\
A_3\beta_2 + B_3\beta_3 + C_3\beta_4 \qquad\quad &= D_3, \\
\cdots & \\
C_J\beta_1 + \qquad\qquad A_J\beta_{J-1} + B_J\beta_J &= D_J.
\end{aligned}$$

In the case of the quadratic spline a similar system of equation, having a coefficient matrix with five nonzero diagonals and three nonzero elements in each corner is obtained. A direct elimination procedure to solve such systems, developed by Gibbons [12] is used in the present code.

C. *Energy conservation.*

As a consequence of the Lagrangian formulation, the present algorithm for advancing particles conserves energy independently of the grid spacing Δx. The expression for the total energy is provided by the Hamiltonian

$$U_{\text{tot}} = \frac{1}{8\pi} \sum_{j,j'=1}^{J} \alpha_j \alpha_{j'} \int_0^L \varphi_{j'}' \varphi_j' \, dx$$

$$+ \frac{1}{8\pi} \sum_{j,j'=1}^{J} (\beta_{yj}\beta_{yj'} + \beta_{zj}\beta_{zj'}) \int_0^L \varphi_{j'}' \varphi_j' \, dx + \frac{1}{2} \sum_{i=1}^{N} m_i (v_{xi}^2 + v_{\perp i}^2). \tag{15}$$

The first term in the right member of Eq. (15) is the electrostatic energy, U_E, the second term is the magnetic energy U_M and the third term is the kinetic energy U_K of the system. This energy conservation applies only to the discrete spatial representation and is therefore exact only in the limit $\Delta t \to 0$.

D. *Implementation*

The finite difference equations for linear and quadratic splines are derived in Appendix A. These equations are written in normalized form with time measured in units of ω_p^{-1}, position in units of the system's length L and the potentials in units of $(m/e)\, L^2 \omega_p^2$. It should be noted that since the algorithm accounts for both the self Coulomb fields and the self-induced fields (neglecting retardation effects), two characteristic lengths, the Debye length $\lambda_D = v_{\text{th}}/\omega_p$ and the collisionless skin depth $\lambda_m = c/\omega_p$, need to be considered. The ratio of these lengths, $\lambda_D/\lambda_m = v_{\text{th}}/c$, which must be sufficiently small to justify the absence of retardation effects, is therefore a significant dimensionless parameter of any computation. Similarly, two characteristic frequencies ω_p and ω_c need to be considered and their ratio ω_c/ω_p is another dimensionless parameter.

Electron energies near 10 KeV correspond to a ratio $v_{\text{th}}/c \simeq 0.11$. This would be a realistic value for energetic electrons in the magnetosphere or for controlled fusion experiments. Values of the ratio ω_c/ω_p in the magnetosphere, in the equatorial region at three Earth radii, are near 0.25. In a number of simulations carried out with this code, the values $v_{\text{th}}/c = 0.33$ and $\omega_c/\omega_p = 0.5$ were chosen to economize computing time, but it is felt that the qualitative results of such computations retain their validity even though these values are 2 to 3 times larger than

realistic values. Computer simulations can rarely duplicate a physical phenomenon with realistic parameters. However it is possible to simulate different aspects of a problem with such parameters that enable the effects we seek to be observed within a reasonable length of computation.

Two versions of the code, using linear and quadratic splines have been written for use on the CDC 7600. These codes use disk storage for particle data (5 words per particle) and runs with up to $5 \cdot 10^5$ particles have been made for the simulation of wavepacket propagation. The computing times are approximately 18 μsec per particle-time step for the linear spline and 26 μsec per particle-time step for the quadratic spline.

3. Effect of Discrete Loading of Parallel Velocities

The first effect considered is the whistler-mode equivalent of the beaming instability encountered in electrostatic problems [11, 13]. It is due to the discrete loading of particles with parallel velocities separated by a finite interval Δv_x. This causes the distribution function to take the form of a sum of δ functions,

$$f(v_x, v_\perp) = \delta(v_\perp - v_{\perp 0}) \sum_{\sigma=-K}^{K} f_0(v_x)\, \delta(v_x - \sigma \Delta v_x)$$

and the dispersion relation, Eq. (1), becomes

$$1 + \left(\frac{kc}{\omega_p}\right)^2 + \frac{\omega_c \Delta v_x}{k} \sum_{\sigma=-K}^{K} \frac{f_0(\sigma \Delta v_x)}{z - \sigma \Delta v_x} + \frac{v_{\perp 0}^2 \Delta v_x}{2} \sum_{\sigma=-K}^{K} \frac{f_0(\sigma \Delta v_x)}{(z - \sigma \Delta v_x)^2} = 0 \qquad (16)$$

where $z = (\omega - \omega_c)/k$. Here the electron distribution has been assumed to be monoenergetic in the perpendicular direction. Each beam gives two roots of the dispersion relation, which are either real or complex conjugates. The complex conjugate roots yield an unstable behavior of the corresponding beam. Since the number of beams is finite it is possible to determine these roots by solving Eq. (16) numerically and the linear behavior of any individual beam may be computed exactly. The result of such a computation is given later in this Section. However, the maximum growth rate may be found analytically by following the method of Dawson [13]. Identities are used to replace the sums over σ in Eq. (16) by integrals over v_x, as in the original dispersion relation, plus singular terms which account for the poles at $z_\sigma = \sigma \Delta v_x$. This analysis yields results similar to those of electrostatic case [11]. For $\Delta v_x \to 0$ and a Maxwellian distribution function

$$f_0 = \exp[-\tfrac{1}{2}(v/v_{\text{th}})^2]/((2\pi)^{1/2}\, v_{\text{th}})$$

the complex frequencies $\omega_\sigma = \alpha_\sigma + i\beta_\sigma$ are given by

$$\alpha_\sigma = \omega_c + \sigma k \Delta v_x + \frac{k\Delta v_x}{2\pi} \tan^{-1}\left(\frac{\zeta_\sigma \operatorname{Im} Z(\zeta_\sigma)}{1 + k^2c^2/\omega_p^2 + \operatorname{Re} Z(\zeta_\sigma)}\right) \tag{17}$$

$$\beta_\sigma = \frac{k\Delta v_x}{2\pi}\left\{\ln \frac{2\pi^2 v_{\perp 0}^2}{(2\pi)^{1/2} v_{\mathrm{th}} \Delta v_x} - \zeta_\sigma^2 - \frac{1}{2}\ln\left[\left(1 + \frac{k^2c^2}{\omega_p^2} - \frac{v_{\perp 0}^2}{2v_{\mathrm{th}}^2} - \left[\frac{\omega_c}{\sqrt{2}\, kv_{\mathrm{th}}} + \frac{v_{\perp 0}^2 \zeta_0}{2v_{\mathrm{th}}^2}\right] \operatorname{Re} Z(\zeta_\sigma)\right)^2 + \left(\left[\frac{\omega_c}{\sqrt{2}\, kv_{\mathrm{th}}} + \frac{v_{\perp 0}^2 \zeta_\sigma}{2v_{\mathrm{th}}^2}\right] \operatorname{Im} Z(\zeta_\sigma)\right)^2\right]\right\} \tag{18}$$

where $\zeta_\sigma = \sigma \Delta v_x/(\sqrt{2}\, v_{\mathrm{th}})$ and $Z(\zeta)$ is the plasma dispersion function [14]. These results show that the natural frequencies α_σ correspond approximately to the Doppler frequencies of the beams, shifted by the cyclotron frequency, while the growth rates β_σ are approximately proportional to the product $k\Delta v_x$.

The dependence of the growth rates β_σ on σ has two relative maxima. The first maximum corresponds to the most intense beam, i.e., the central beam $\sigma = 0$ for a Maxwellian distribution. The frequency and growth rate for this mode are obtained by setting $\zeta_\sigma = 0$ in Eqs. (17) and (18) which gives a frequency $\alpha_{\sigma=0} = \omega_c$ equal to the cyclotron frequency. The second maximum corresponds to the beam closest to the resonant velocity $v_R = (\omega_0 - \omega_c)/k$ for which the frequency lies close to the whistler frequency ω_0. This second relative maximum is significant only in the case of a large population of resonant electrons and, except for this case, the first relative maximum, corresponding to $\sigma = 0$, may therefore be taken as an estimate of the maximum growth rate. For example, with $kc/\omega_p = 1/\sqrt{3}$, $\omega_c = \omega_p/2$ and $v_{\perp 0}/v_{\mathrm{th}} = \sqrt{2}$ (i.e., $T_\perp = T_\parallel$) Eq. (18) gives $\beta_{\sigma=0} = 0.041\omega_p$ for $v_{\mathrm{th}} = c/3$ and $\beta_{\sigma=0} = 0.025\omega_p$ for $v_{\mathrm{th}} = c/4.5$ [15]. The growth rates obtained from numerical solutions of the dispersion relation, Eq. (16), for the above examples are given in Table I. For $v_{\mathrm{th}} = c/3$ the relative maxima which would occur at $\omega_c = 0.5\omega_p$ and $\omega_0 = 0.13\omega_p$ are very broad and merge into a single wide spectrum. Because of the large number of resonant particles in this case, the growth rate near $\alpha_{\sigma=3} = \omega_0 = 0.13\omega_p (\beta_{\sigma=3} = 0.047\omega_p)$ is somewhat larger than the above estimate ($\beta_{\sigma=0} = 0.041\omega_p$) but the difference remains small. For $v_{\mathrm{th}} = c/4.5$, fewer resonant electrons are present, and both maxima are evident. The maximum near $\alpha_{\sigma=0} = \omega_c$ clearly dominates and agrees with the estimated maximum.

A test was carried out to observe in some detail the occurrence of the beaming instability with the above parameters in the case $v_{\mathrm{th}} = c/3$. The particles in this test were loaded uniformly in x with $\Delta x = L/64$ and $\Delta v_x = c/5$ (11 beams). In the perpendicular direction the distribution was monoenergetic and uniform in phase

TABLE I

Roots of the Dispersion Relation, Eq. (16), for the Whistler Beaming Instability with $kc/\omega_p = 1/\sqrt{3}$, $\omega_c/\omega_p = 1/2$, $\Delta v_x = c/5$, $T_\perp = T_\parallel$ and Two Values of the Thermal Velocity, $v_{th} = c/3$ and $v_{th} = c/4.5$

	$v_{th} = c/3$		$v_{th} = c/4.5$	
σ	α_σ/ω_p	β_σ/ω_p	α_σ/ω_p	β_σ/ω_p
−5	1.077	6.23×10^{-3}	1.077	3.20×10^{-4}
−4	0.961	1.28×10^{-2}	0.962	1.85×10^{-3}
−3	0.842	2.16×10^{-2}	0.846	6.85×10^{-3}
−2	0.721	3.06×10^{-2}	0.726	1.60×10^{-2}
−1	0.597	3.79×10^{-2}	0.599	2.44×10^{-2}
0	0.472	4.23×10^{-2}	0.468	2.45×10^{-2}
1	0.347	4.38×10^{-2}	0.343	3.03×10^{-3}
2	0.227	4.46×10^{-2}	0.241	0
3	0.120	4.66×10^{-2}	0.123	1.13×10^{-2}
4	0.028	3.27×10^{-2}	0.037	5.95×10^{-3}
5	−0.079	1.36×10^{-2}	−0.077	7.06×10^{-4}

angles with $\Delta\theta = 2\pi/64$. This choice of Δx and $\Delta\theta$ reduces as much as possible other numerical effects described in Sections IV and V, while Δv_x is purposely chosen rather large to emphasize the beaming instability. An initial perturbation is applied to the central set of beams, which gives to this set of beams a small-amplitude circularly polarized perpendicular velocity,

$$\tilde{v}_\sigma(x, t = 0) = \begin{cases} \tilde{v}_\perp{}^0(\hat{\mathbf{y}} \cos kx + \hat{\mathbf{z}} \sin kx) & \text{for } \sigma = 0, \\ 0 & \text{for } \sigma \neq 0, \end{cases}$$

with $\tilde{v}_\perp{}^0 = v_{\perp 0}/40$.

The central-beam perturbation as a function of time for this test is given in Fig. 5. The solid line shows the result of a Laplace transform solution in time of the linearized equations for $2K + 1$ beams with a spatial dependence of the form $\exp(ikx)$. This solutions is obtained from the $2(2K + 1)$ roots of Eq. (16), 22 roots in this case, superimposing the corresponding modes with their proper initial excitation and evaluating the time behavior of the combination. The circles give the results of the simulation code and the broken line shows the maximum growth rate ($\beta_{\sigma=0} = 0.041\omega_p$) obtained analytically.

The results of this test may be interpreted as follows. The current due to the central beam perturbation produces circularly polarized fields which drive the off-center beams of the plasma, causing them to acquire circularly polarized velocity perturbations and causing the perturbation of the central beam to decrease initially.

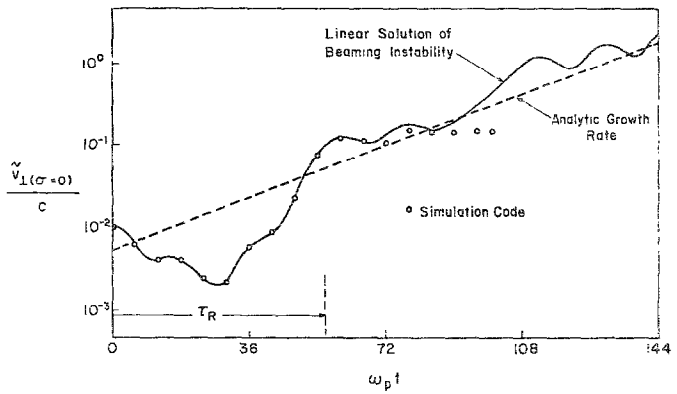

FIG. 5. Test problem showing the effect of discrete loading of particles in parallel velocity.

The perturbations of the off-center beams grow at the exponential rates β_e but are at first phase mixed since they advance with different velocities. However, as the recurrence time $\tau_R = 2\pi/k\Delta v_x = 54\omega_p^{-1}$ is approached these perturbations come back into phase producing strong fields which drive the central beam perturbation to a large value as shown in Fig. 5 near $t = 54\omega_p^{-1}$. The magnetic energy drops initially from $U_M = 0.7 \times 10^{-4} U_{\text{tot}}$ at $t = 0$ to $U_M = 0.7 \times 10^{-6} U_{\text{tot}}$ at $t = 43\omega_p^{-1}$, then regrows as t approaches τ_R to reach a maximum $U_M = 2.2\ 10^{-3} U_{\text{tot}}$ at $t = 58\omega_p^{-1}$. Note that the simulation results in Fig. 5 level off for $t > 80\omega_p^{-1}$. At this time the velocity perturbation in the x direction has reached a value $\delta v_x \simeq 0.1c$ equal to half the beam separation. This causes the beams to merge and linear theory is no longer expected to hold.

IV. Effect of Discrete Loading of Perpendicular Velocity Phases

The effect of initializing the particles with perpendicular velocities having discrete phase angles, separated by a finite interval $\Delta\theta$ is considered in this section. This effect has no equivalent in purely electrostatic simulations. The electron distribution is again assumed to be monoenergetic in the perpendicular direction, with perpendicular velocities uniformly distributed at M values $\theta_\mu = 2\pi\mu/M$ of the phase angle, with $\mu = 1,..., M$, and may be considered as M separate beams. Each beam is perturbed by the whistler wave and has a charge density perturbation $\rho^\mu(x)$. If

$$\rho^\mu(x) = \tilde{\rho}^0 \sin(kx - 2\pi\mu/M),$$

where k is the whistler wavenumber. In this case the perturbations would cancel each other and the total charge density would be uniform. In the simulation code, however, the charge density is computed only at discrete grid point in the x direction and this results in an incomplete cancellation of the charge densities which results in the excitation of electrostatic modes.

This effect may be understood in terms of the simple example illustrated in Fig. 6, involving two beams $\mu = 1$ and $\mu = 2$ and four particles in each beam,

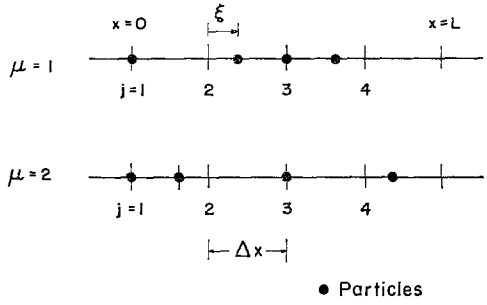

FIG. 6. Example illustrating the effect of discrete loading of particles in perpendicular velocity phase angles.

each with a charge $-en_0L/8$ initially located at four grid points $j = 1, 2, 3, 4$. After some time has elapsed the particles of the first beam, $\mu = 1$, have acquired sinusoidal displacements in the x direction due to the $\mathbf{v}_\perp \times \mathbf{B}_\perp$ force. Particles at $j = 2$ and 4 undergo the maximum displacement ξ and particles at $j = 1$ and 3 have zero displacements. The charge sharing scheme, using the linear spline, then yields charge densities at the grid points given by the vector

$$\rho_j^{\mu=1} = (-en_0/2)\{1, 1 - \epsilon, 1 + 2\epsilon, 1 - \epsilon\}.$$

where $\epsilon = \xi/\Delta x$. The particles of the second beam, $\mu = 2$, acquire displacements which are 180° out of phase from those of the first beam and the charge densities for this beam are given by

$$\rho_j^{\mu=2} = (-en_0/2)\{1 + 2\epsilon, 1 - \epsilon, 1, 1 - \epsilon\}.$$

The total charge density at each grid point, obtained by taking the sum of these vectors is then

$$\rho_j = -en_0\{1 + \epsilon, \quad 1 - \epsilon, \quad 1 + \epsilon, \quad 1 - \epsilon\},$$

in which a second harmonic with amplitude $\tilde{\rho}_2 = -en_0\xi_0/\Delta x$ is superimposed over

the uniform charge. Since only the uniform charge is neutralized by the ion background, second harmonic electrostatic modes are excited in the plasma.

In the general case the position of a particle is given by

$$x^{j\sigma\mu} = j\Delta x + \sigma\Delta v_x t + \xi^{j\sigma\mu} \tag{19}$$

where the displacement $\xi^{j\sigma\mu}$ due to the interaction with the whistler wave is of the form

$$\xi^{j\sigma\mu} = \xi^{\sigma} \sin[2\pi((\mu/M) - (j/J))]. \tag{19a}$$

Here the superscripts j, σ and μ define respectively the initial position, parallel velocity and phase angle of the particle and J is the number of grid points per whistler wavelength. This expression is introduced into the charge density term of Eq. (8) to give

$$\begin{aligned} \rho_{j'} &= \frac{1}{\Delta x} \sum_{i=1}^{N} q_i \varphi(x_i - j'\,\Delta x), \\ &= -\frac{en_R}{M} \sum_{j,\mu} \varphi[\xi^{j\sigma_R\mu} - (j - j')\,\Delta x]. \end{aligned} \tag{20}$$

Here n_R denotes the resonant particle density and $\sigma_R \simeq v_R/\Delta v_x$. Since resonant particles undergo large displacements they are the major contributors to the present effect and nonresonant particles have been neglected in Eq. (20). Substituting Eq. (19a) into Eq. (20) and taking a discrete Fourier transform with respect to j' yields, as shown in Appendix B,

$$\bar{\rho}_n = \begin{cases} -en_R \sum_{\substack{p=-\infty \\ r=r_0+qJ/M}}^{+\infty} J\bar{\varphi}_{-n+pJ} J_{rM}(z_p)\, e^{-2\pi i(n-pJ)v_R t/L} & \text{for} \quad n = r_0 M + q_0 J, \\ 0 & \text{for} \quad n \neq r_0 M + q_0 J. \end{cases} \tag{21}$$

Here p, q, q_0, r, r_0 must be integers, $z_p = 2\pi(n - pJ)\,\xi_R/L$ where ξ_R is the maximum displacement of resonant electrons, J_ν denotes the Bessel function of the first kind of integer order and $\bar{\varphi}_m$ is the Fourier transform of the base function defined in Appendix B.

Nonzero harmonics occur with order $n = r_0 M + q_0 J$ where r_0 and q_0 are arbitrary integers. For example, with $J = 16$ and $M = 12$, electrostatic modes corresponding to the 4-th and 8-th harmonic are driven. With $J = M$ no electrostatic mode harmonics are driven. The magnitude of $\bar{\rho}_n$ may be estimated as

$$\bar{\rho}_n \simeq en_R[(\omega_T t)^2/2\chi_{r_0 M}]^{b+1}\, J_{r_0 M}(\chi_{r_0 M}) \tag{22}$$

where ω_T is the trapping frequency, $\chi_{r_0 M}$ is the value of z for which $J_{r_0 M}(z)$ reaches

its first maximum, $b = 1$ for the linear spline and $b = 2$ for the quadratic spline. This estimate, which is valid for $\omega_T t \lesssim \pi$ is derived in Appendix B.

Numerical simulations of cyclotron damping with linear and quadratic base functions have been carried out to illustrate this effect. In these runs a whistler wave with $kc/\omega_p = 1/\sqrt{3}$ was initialized in a Maxwellian plasma with $v_{th} = c/3$, $v_{\perp 0} = \sqrt{2}\, v_{th}$ (monoenergetic in the perpendicular direction) and $\omega_c = \omega_p/2$. The initial magnetic energy is $U_M = 4.9 \times 10^{-5} U_{tot}$ and the initial trapping frequency is $\omega_T = 4.5 \times 10^{-2} \omega_p$. From $t = 0$ to $t = 50\omega_p^{-1}$ the magnetic energy is observed to decay at the rate ($2\gamma = 0.035\omega_p$) predicted by linear theory. This aspect of the simulation will be discussed in Section V and only the electrostatic energy, which would be zero in this case for a continuous plasma is considered now. For $J = M = 16$ the electrostatic energy remains negligible. However, for $J = 16$, $M = 12$ the electrostatic energy increases as shown in Fig. 7 and resides entirely in modes $n = 4$ and 8.

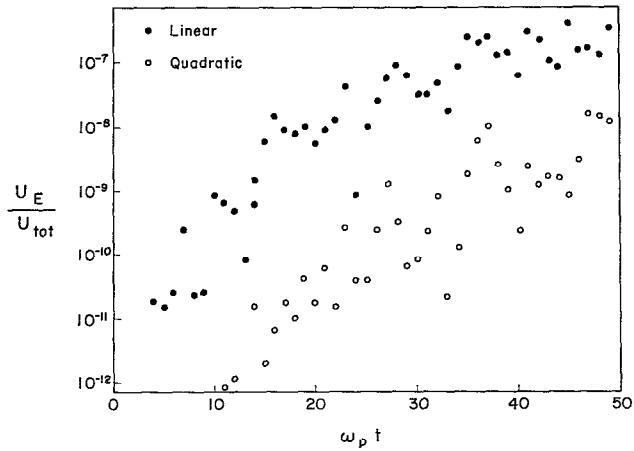

FIG. 7. Excitation of electrostatic modes due to discrete loading of particles in perpendicular velocity phase angles.

These results are in agreement with Eq. (21). Assuming a resonant particle density $n_R = 0.05 n_0$, estimates of the ratio of electrostatic energy at $t = 50\omega_p^{-1}$ to total energy, obtained from Eq. (22), are $U_E/U_{tot} \simeq 10^{-7}$ for the linear base function and $U_E/U_{tot} \simeq 0.4 \times 10^{-8}$ for the quadratic base function. These estimates agree qualitatively with the values observed in Fig. 7.

5. Effect of Discrete Spatial Loading

The effect of regular loading of the particles at the grid points in the x direction is considered now. Assume that a whistler wave with mode number n propagates

through the plasma. As particles travel along this wave, their perpendicular velocities acquire perturbations with a spatial dependence of the form

$$\tilde{v}_\perp = \tilde{v}_\perp{}^0 e^{2\pi i n x/L},$$

where the real part represents the y component of the velocity perturbation and the imaginary part represents its z component. Suppose that at some time t the particles of a given beam σ fall exactly at the grid points as shown in Fig. 8a. The transverse

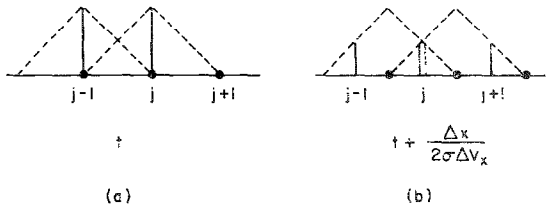

FIG. 8. Example illustrating the effect of discrete spatial loading of the particles.

current density at grid point j (for the linear spline) is due only to the particle at this point. This current density is

$$J_{\perp j}(t) = -en_0\tilde{v}_\perp{}^0 e^{2\pi i n j/J}.$$

At a later time $t + \tau_\sigma/2$, where $\tau_\sigma = \Delta x/\sigma\Delta v_x$ the particles will have drifted so that they are located midway between grid points as shown in Fig. 8b. The current density at grid point j is now the sum of contributions from two particles,

$$\begin{aligned} J_{\perp j}(t + \tau_\sigma/2) &= -(en_0\tilde{v}_{\perp 0}/2)(e^{-\pi i n\Delta x/L} + e^{\pi i n\Delta x/L})\, e^{2\pi i n j/J} \\ &= -en_0\tilde{v}_{\perp 0} e^{2\pi i n j/J}\cos(\pi n/J), \end{aligned}$$

and is smaller than the current at time t. Thus as particles drift across the grid points the magnitude of the current fluctuates and these fluctuations drive new waves with the same mode number n as the original wave but with frequencies $\omega_\sigma = 2\pi/\tau_\sigma$.

When all the beams (i.e., all values of σ) are considered there results a phase mixing so that the vector potential $\tilde{\beta}_n{}^g$ due to this effect remains small, except at times which are multiples of the "beat time" $\tau_B = \Delta x/\Delta v_x$. At these times the contributions of all the beams are in phase and large deviations occur.

This effect may be analyzed by a perturbation method presented in Appendix C. Consider the simulation of a whistler wave with mode number n, amplitude $\tilde{\beta}_n{}^w$,

frequency ω_0 and damping constant γ_0. The vector potential deviation due to discrete spatial loading is given by

$$\frac{\bar{\beta}_n{}^g}{\bar{\beta}_n{}^w} = \frac{\omega_x{}^2}{k^2c^2}\frac{\omega_0}{\omega_c}k^2v_{\perp 0}^2\left(\frac{n}{J}\right)^b\sum_\sigma A_\sigma\cos(\omega_\sigma t + b\pi/2), \tag{23}$$

where $\omega_\sigma = 2\pi\sigma\Delta v_x/\Delta x$,

$$A_\sigma = \frac{n_\sigma[(1 + i\Omega_\sigma t)\,e^{-i\Omega_\sigma t} - e^{-\gamma_0 t}]\,e^{i\omega_0 t}}{\Omega_\sigma{}^2}, \tag{24}$$

$$\Omega_\sigma = \omega_0 - \omega_c - k\sigma\Delta v_x\,,$$

$b = 1$ for the linear spline and $b = 2$ for the quadratic spline.

This effect is evident in the behavior of the magnetic energy for the cyclotron damping simulation shown in Fig. 9, which corresponds to the run described at the

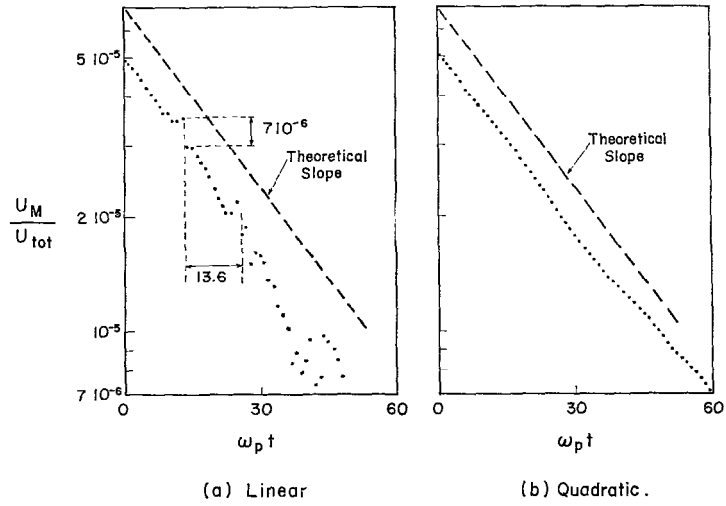

FIG. 9. Deviation in magnetic energy from cyclotron damping due to discrete spatial loading of the particle.

end of Section 4. In this case $\Delta v_x/c = 1/20$ from which $\tau_B = 13.6\omega_p^{-1}$ and Eq. (23) gives

$$\frac{\Delta U_{Mn}}{U_{Mn}} = 2\frac{|\,\bar{\beta}_n{}^g\,|}{|\,\bar{\beta}_n{}^w\,|} \simeq 0.16 \text{ (linear spline)},$$

$$\simeq 0.01 \text{ (quadratic spline)}.$$

The deviations from cyclotron damping evident in Fig. 9 agree both in magnitude and frequency of occurrence with the above results, and are smaller, by at least an order of magnitude, for the quadratic spline than for the linear spline.

6. Conclusions

A study of discrete particle effects in whistler simulation has been made using algorithms derived by the variational method of Ralph Lewis. This method provides a systematic procedure whereby the proper charge sharing scheme for the particles is derived in terms of the spline used in the interpolation of the potentials to yield energy-conserving algorithms. This perfect energy conservation (in the limit $\Delta t \to 0$) is unfortunately not accompanied by perfect momentum conservation and such algorithms are not necessarily optimal. However, in the electrostatic case, energy-conserving algorithms of this type have been studied extensively [16, 17] and found satisfactory in simulations of small-amplitude phenomena [18]. Their application to whistler simulation appears therefore as a natural extension of these earlier studies.

Numerical effects due to the discrete initial loading of the particles in parallel velocities, perpendicular velocity phase angles and positions have been analysed in Sections 3, 4 and 5 respectively. The results of numerical tests have been presented to confirm the analytical results and the performance of two versions of the algorithm based on linear and quadratic splines have been compared.

The effect of discrete loading in parallel velocities, i.e., the finite velocity increment Δv_x, considered in Section 3, is the appearance of recurrence and of a whistler-mode beaming instability. As in the electrostatic mode, the recurrence time is $\tau_R = 2\pi/k\Delta v_x$ and the growth rate of the instability scales approximately as $k\Delta v_x$, where k is the mode number considered. Sufficiently small values of Δv_x must be used to keep this effect under control. Values of Δv_x ranging from $c/40$ to $c/20$ with $v_{th}/c = 1/3$ have been used in a number of simulations without adverse effects from recurrence or beaming instability. It should be noted that small values of Δv_x not only lengthen the recurrence time and decrease the beaming instability growth rate, but also reduce the saturation level of the instability. This occurs when adjacent beams merge due to either the whistler wave being studied or the beaming instability itself.

The effect of discrete loading in perpendicular velocity phases, i.e., the finite phase increment $\Delta\theta$ was considered in Section IV. This effect causes density fluctuations which drive electrostatic modes and may modify the whistler wave itself. The magnitude of these fluctuations is given by Eq. (22), where $M = 2\pi/\Delta\vartheta$ is the number of phase values, and is significantly smaller for the quadratic spline than for the linear spline. In the case of a nearly monochromatic whistler wave, a

value of M close to the number J of intervals Δx per whistler wavelength is optimal since this effect vanishes for $M = J$. For distribution functions having a finite energy spread in the perpendicular direction it is possible to stagger the angles θ_μ by phase-shifting the particles by an angle $\Delta\theta/2$ on alternate concentric circles, instead of aligning them radially as shown in Fig. 2(b). This causes a partial phase mixing of the density fluctuations thereby reducing their amplitude without disrupting the quiet start.

The effect of spatial loading at discrete intervals Δx, discussed in Section 5, is the appearance of fluctuations in the magnetic vector potential. These fluctuations are described by Eqs. (23) and (24) and, because of phase mixing between beams, remain small except at time intervals $\tau_n = \Delta x/\Delta v_x$ for which the perturbations of all beams are in phase. This effect may be controlled by choosing sufficiently small values of Δx and Δv_x and is also significantly smaller for the quadratic spline than for the linear spline. Typical values of Δx equal to $\frac{1}{16}$th of the shortest wavelength of interest, with $\Delta v_x = c/40$ to $c/20$ for $v_{\text{th}} = c/3$ have been found satisfactory.

The results of Section 4 and 5 show that the quadratic spline is significantly superior to the linear spline for the simulation of low-amplitude waves. These results also suggest that higher-order splines, having Fourier coefficients $\bar{\varphi}_n$ dropping more steeply as n increases may yield further improvement. This improvement, however, would have to be weighted against the increased complexity of the computations.

In the simulation of large-amplitude whistlers the discrete particle effects discussed in this paper become less important because the perturbations they generate remain small compared to the whistler wave itself. The advantage of the quadratic spline over the linear spline becomes less obvious in this case. This conclusion has been confirmed in simulations similar to the example of Sections 4 and 5 but with a larger amplitude giving a trapping frequency $\omega_T = 0.2\omega_p$.

APPENDIX A: FINITE DIFFERENCE EQUATIONS

The finite-difference equations are written in normalized form with time measured in units of ω_p^{-1}, position in units of the system's length L and the potentials in units of $(m/e)\,L^2\omega_p^2$. The system's length L is related to the collisionless skin depth c/ω_p by the dimensionless ratio $k_M = L\omega_p/c$.

1. *Linear Spline*

Let j denote the closest grid point to the left of x_i and let $p_i = (x_i - j\Delta x)/\Delta x$, $0 \leqslant p_i < 1$. Eqs. (6), (8), (10a), and (13) take respectively the form

$$dv_{xi}/dt = -J[\alpha_j - \alpha_{j+1} + k_M v_{yi}(\beta_{yj+1} - \beta_{yj}) + k_M v_{zi}(\beta_{zj+1} - \beta_{zj})],$$

$$\alpha_{j-1} - 2\alpha_j + \alpha_{j+1} = -(\rho_0 + \rho_j)/J^2,$$
$$A_{\perp i} = (1 - p_i)\,\beta_j + p_i\beta_{j+1},$$
$$A_j\beta_{j-1} + B_j\beta_j + C_j\beta_{j+1} = D_j,$$

where

$$A_j = 1 - \Gamma\rho'_{j-1}, \qquad C_j = 1 - \Gamma\rho_j',$$
$$B_j = -2 - \Gamma\rho''_j, \qquad D_j = -\Gamma\sigma_j,$$

and $\Gamma = k_M^2/J^2(1 + i\delta_e)$. Each particle i, with $j \leqslant x_i/\Delta x < j + 1$, contributes the following increments to the arrays ρ_j, ρ_j', ρ''_j and σ_j,

$$\Delta\rho_j = -J(1 - p_i)\,Z_i, \qquad \Delta\rho_{j+1} = -Jp_iZ_i,$$
$$\Delta\rho_j' = -Jp_i(1 - p_i)\,Z_i, \qquad \Delta\rho''_j = -J(1 - p_i)^2\,Z_i, \qquad \Delta\rho''_{j+1} = -Jp_i^2Z_i$$
$$\Delta\sigma_j = -J(1 - p_i)\,h_iZ_i, \qquad \Delta\sigma_{j+1} = -Jp_ih_iZ_i,$$

where Z_i represents the particle weight with the normalization $\sum_{i=1}^{N} Z_i = 1$.

2. *Quadratic Spline*

The second derivative operator takes the form

$$\int_0^L \varphi'(x - j\Delta x)\,\varphi'(x - j'\Delta x)\,dx = \begin{cases} 1/\Delta x & \text{for} \quad j' - j = 0 \\ -1/3\Delta x & \text{for} \quad |j' - j| = 1 \\ -1/6\Delta x & \text{for} \quad |j' - j| = 2 \\ 0 & \text{for} \quad |j' - j| > 2 \end{cases}$$

Let j denote the grid point closest to x_i and let $p_i = (x_i - j\Delta x)/\Delta x$, $-\frac{1}{2} \leqslant p_i < \frac{1}{2}$. Equations (6), (8), (10a) and (13) become, respectively,

$$\frac{dv_{wi}}{dt} = -J\{(\tfrac{1}{2} - p_i)\,\alpha_{j-1} + 2p_i\alpha_{j'} - (\tfrac{1}{2} + p_i)\,\alpha_{j+1}$$
$$+ k_Mv_{yi}[-(\tfrac{1}{2} - p_i)\,\beta_{yj-1} - 2p_i\beta_{yj} + (\tfrac{1}{2} + p_i)\,\beta_{yj+1}]$$
$$+ k_Mv_{zi}[-(\tfrac{1}{2} - p_i)\,\beta_{zj-1} - 2p_i\beta_{zj} + (\tfrac{1}{2} + p_i)\,\beta_{zj+1}]\}$$
$$\alpha_{j-2} + 2\alpha_{j-1} - 6\alpha_j + 2\alpha_{j+1} + \alpha_{j+1} = -6(\rho_0 + \rho_j)/J^2,$$
$$A_{\perp i} = \tfrac{1}{2}(\tfrac{1}{2} - p_i)^2\,\beta_{j-1} + (\tfrac{3}{4} - p_i^2)\,\beta_j + \tfrac{1}{2}(\tfrac{1}{2} + p_i)^2\,\beta_{j+1}$$
$$A_j\beta_{j-2} + B_j\beta_{j-1} + C_j\beta_j + D_j\beta_{j+1} + E_j\beta_{j+2} = F_j,$$

where

$$A_j = -\tfrac{1}{6}\Gamma\rho'''_{j-2}, \qquad D_j = -\tfrac{1}{3} + \Gamma\rho''_j,$$
$$B_j = -\tfrac{1}{3} + \Gamma\rho''_{j-1}, \qquad E_j = -\tfrac{1}{6} + \Gamma\rho'''_j,$$
$$C_j = 1 + \Gamma\rho'_j, \qquad F_j = -\Gamma\sigma_j .$$

Each particle i, with $j - \frac{1}{2} \leqslant x_i/\Delta x < j + \frac{1}{2}$, contributes the following increments to the arrays ρ_j, ρ'_j, ρ''_j, ρ'''_j and σ_j,

$$\Delta\rho_{j-1} = -\frac{J}{2}(\tfrac{1}{2} - p_i)^2 Z_i, \qquad \Delta\sigma_{j-1} = -\frac{J}{2}(\tfrac{1}{2} - p_i)^2 h_i Z_i,$$

$$\Delta\rho_j = -J(\tfrac{3}{4} - p_i^2) Z_i, \qquad \Delta\sigma_j = -J(\tfrac{3}{4} - p_i^2) h_i Z_i,$$

$$\Delta\rho_{j+1} = -\frac{J}{2}(\tfrac{1}{2} + p_i)^2 Z_i, \qquad \Delta\sigma_{j+1} = -\frac{J}{2}(\tfrac{1}{2} + p_i)^2 h_i Z_i,$$

$$\Delta\rho'_{j-1} = -\frac{J}{4}(\tfrac{1}{2} - p_i)^4 Z_i, \qquad \Delta\rho''_j = -\frac{J}{2}(\tfrac{1}{2} + p_i)^2 (\tfrac{3}{4} - p_i^2) Z_i,$$

$$\Delta\rho'_j = -J(\tfrac{3}{4} - p_i^2)^2 Z_i, \qquad \Delta\rho''_{j-1} = -\frac{J}{2}(\tfrac{1}{2} - p_i)^2 (\tfrac{3}{4} - p_i^2) Z_i,$$

$$\Delta\rho'_{j+1} = -\frac{J}{4}(\tfrac{1}{2} + p_i)^4 Z_i, \qquad \Delta\rho'''_{j-1} = -\frac{J}{4}(\tfrac{1}{4} - p_i)^2 Z_i .$$

APPENDIX B: Electrostatic Modes Amplitudes

Taking the discrete Fourier transform of Eq. (20) yields

$$\bar{\rho}_n = \frac{1}{J}\sum_{j'} \rho_{j'} e^{-2\pi i n j'/J}$$
$$= -\frac{en_R}{JM}\sum_{j,j',\mu} \varphi(x^{j\sigma_R\mu} - j'\Delta x)\, e^{-2\pi i n j'/J}. \tag{B1}$$

Let

$$\bar{\varphi}_n = \frac{1}{L}\int_{-L/2}^{L/2} \varphi(x)\, e^{-2\pi i n x/L}\, dx = \frac{1}{J}\left[\frac{\sin(\pi n/J)}{\pi n/J}\right]^{b+1}$$

denote the Fourier transform vector of the spline, where $b = 1$ for the linear spline and $b = 2$ for the quadratic spline, then

$$\varphi(x^{j\sigma_R\mu} - j'\Delta x) = \sum_{n'} \bar{\varphi}_{n'} e^{2\pi i n'(x^{j\sigma_R\mu} - j'\Delta x)/L}.$$

Substituting this expression and Eq. (19) into Eq. (B1) and carrying out the sum over j' yields

$$\bar{\rho}_n = -\frac{en_R}{M} \sum_{p,j,\mu} \bar{\varphi}_{-n+pJ} e^{-2\pi i(n-pJ)v_R t/L} e^{-2\pi i n j/J} \exp\left\{ iz_p \left[2\pi \left(\frac{\mu}{M} - \frac{j}{J} \right) \right] \right\}. \quad \text{(B2)}$$

where $z_p = 2\pi(n - pJ)\,\bar{\xi}_R/L$, and $\bar{\xi}_R$ is the maximum displacement of resonant electrons. The last exponential factor in Eq. (B2) is now expanded using the identity

$$\exp\{iz \sin \psi\} \equiv \sum_{\nu} J_\nu(z)\, e^{i\nu\psi}$$

where $J_\nu(z)$ denotes the Bessel function of the first kind of integer order [19]. After substituting this identity into Eq. (B2), the sum over μ may be carried out to give

$$\bar{\rho}_n = -en_R \sum_{p,r,j} \bar{\varphi}_{-n+pJ} e^{-2\pi i(n-pJ)v_R t/L} J_{rM}(z_p)\, e^{-2\pi i(n+rM)j/J}.$$

The sum over j vanishes, except for $n + rM = qJ$, where q is an integer. Thus $\bar{\rho}_n \neq 0$ only for $n = r_0 M + q_0 J$ where r_0 and q_0 are integers and Eq. (21) follows.

An estimate of $\bar{\rho}_n$ may be obtained by retaining only the largest term in the sums over p and q in Eq. (21). This term corresponds to $r = r_0$, i.e., to the lowest-order Bessel function, and to a value of z_p corresponding to the first maximum, $\chi_{r_0 M}$, of the Bessel function $J_{r_0 M}$. The maximum displacement of resonant electrons is given by $\bar{\xi}_R \simeq L(\omega_T t)^2/4\pi$ for $\omega_T t \lesssim \pi$ where ω_T is the trapping frequency. Thus the largest term in the sum over n corresponds to

$$-n + pJ \simeq 2\chi_{r_0 M}/(\omega_T t)^2.$$

Retaining only these values of r and $-n + pJ$ in Eq. (21) yields Eq. (22).

APPENDIX C: Derivation of Eqs. (23) and (24)

Consider a particle initially loaded at $j\Delta x$, with parallel velocity $\sigma\Delta v_x$ and perpendicular velocity phase angle $\mu\Delta\theta$. A monoenergetic velocity distribution in the perpendicular direction is assumed with perpendicular velocity $v_{\perp 0}$. The position and velocities of this particle at time t are given by

$$x^{j\sigma\mu} = j\Delta x + \sigma\Delta v_x t + \xi^{j\sigma\mu}, \quad \text{(C1)}$$

$$v_x^{j\sigma\mu} = \sigma\Delta v_x + \dot{\xi}^{j\sigma\mu}, \quad \text{(C2)}$$

$$v_\perp^{j\sigma\mu} = v_{\perp 0} e^{i(\mu\Delta\theta + \omega_c t)} + \eta^{j\sigma\mu}. \quad \text{(C3)}$$

where $\xi^{j\sigma\mu}(t)$ denotes the displacement of the particle due to interaction with the whistler wave and $\eta^{j\sigma\mu}(t)$ denotes its perpendicular velocity perturbation. Complex notations are used to denote $v_\perp^{j\sigma\mu}$ and $\eta^{j\sigma\mu}$ with the real and imaginary parts along the y and z directions, respectively.

The parallel component of the Lorentz force yields

$$\ddot{\xi}^{j\sigma\mu} = -\frac{ev_{\perp 0}}{mc}\left[\frac{\partial A_y}{\partial x}\cos(\mu\Delta\theta + \omega_c t) + \frac{\partial A_z}{\partial x}\sin(\mu\Delta\theta + \omega_c t)\right]_{x=j\Delta x+\sigma\Delta v_x t} \tag{C4}$$

where $A(x, t)$ is defined in Eq. (4). Introducing the Fourier transform $\bar{\varphi}_n$ of the spline defined in Appendix B yields

$$\frac{\partial A}{\partial x}\bigg|_{j\Delta x+\sigma\Delta v_x t} = \frac{2\pi i}{L}\sum_n nJ\bar{\varphi}_n\bar{\beta}_n e^{2\pi inj/J}e^{2\pi in\sigma\Delta v_x t/L}$$

where

$$\bar{\beta}_n = \frac{1}{J}\sum_j \beta_j e^{-2\pi inj/J}$$

is the discrete Fourier transform of β_j. Substituting this expression into Eq. (C4) and taking the Laplace transform defined by

$$\hat{g}(\omega) = \int_0^\infty g(t)\, e^{i\omega t}\, dt$$

gives

$$\hat{\xi}^{j\sigma\mu} = \frac{ev_{\perp 0}}{mc}\frac{\pi}{L\omega^2}\sum_{\substack{n\\ \nu=\pm 1}} Jn\bar{\varphi}_n e^{2\pi inj/J}e^{i\nu\mu\Delta\theta}$$
$$\times\left[i\tilde{\bar{\beta}}_{yn}(\omega + \omega_{n\sigma} + \nu\omega_c) + \nu\tilde{\bar{\beta}}_{zn}(\omega + \omega_{n\sigma} + \nu\omega_c)\right] \tag{C5}$$

where $\omega_{n\sigma} = 2\pi n\sigma\Delta v_x/L$.

The perpendicular canonical momentum equation yields

$$\frac{d}{dt}\left(v_\perp^{j\sigma\mu} - \frac{e}{mc}A\right) = i\omega_c v_\perp^{j\sigma\mu}.$$

and after transformations this equation gives

$$\hat{\eta}^{j\sigma\mu} = \frac{e}{mc}\frac{\omega}{\omega + \omega_c}\sum_n J\bar{\varphi}_n e^{2\pi inj/J}\hat{\bar{\beta}}_n(\omega + \omega_{n\sigma}). \tag{C6}$$

The perpendicular current density at grid point j' is given by

$$J_{\perp j'} = -\frac{en_0}{M} \sum_{j,\sigma,\mu} n_\sigma v_\perp^{j\sigma\mu} \varphi(x^{j\sigma\mu} - j'\Delta x)$$

where $n_\sigma = f_0(\sigma \Delta v_x)\, \Delta v_x$ is the relative particle density of beam σ. This expression is manipulated by taking the Fourier transform with respect to j', substituting Eqs. (C1) and (C3), linearizing with respect to the small quantities $\xi^{j\sigma\mu}$ and $\eta^{j\sigma\mu}$ and taking the Laplace transform with respect to t. These operations yield

$$\hat{\bar{J}}_n(\omega) = -\frac{en_0}{M} \sum_{j,\sigma,\mu,p} n_\sigma \bar{\varphi}_{-n+pJ} \left[\hat{\eta}^{j\sigma\mu}(\omega + \omega_{(-n+pJ)\sigma}) + \frac{2\pi i(-n+pJ)}{L} v_{\perp 0} e^{i\mu\Delta\theta} \hat{\xi}^{j\sigma\mu}(\omega + \omega_{(-n+pJ)\sigma} + \omega_c)\right].$$

Substituting Eqs. (C5) and (C6) and carrying out the sums over j and μ gives

$$\hat{\bar{J}}_n(\omega) = \frac{\omega_p^2}{4\pi c} \sum_{\sigma,p,q} n_\sigma J^2 \bar{\varphi}_{-n+pJ} \bar{\varphi}_{n+qJ} \left[\frac{\omega + \omega_{(-n+pJ)\sigma}}{\omega + \omega_{(-n+pJ)\sigma} + \omega_c} + \frac{4\pi^2(-n+pJ)(n+qJ)}{L^2} \frac{v_{\perp 0}^2}{2} \frac{1}{(\omega + \omega_{(-n+pJ)\sigma} + \omega_c)^2}\right] \times \hat{\bar{\beta}}_n(\omega + \omega_{(p+q)J\sigma}). \tag{C7}$$

The term corresponding to $p = q = 0$ in Eq. (C7) is the current density associated with the whistler wave. The other terms are perturbations due to the discrete nature of the field representation and of the initial particle loading. Let the sum of these terms be denoted as $\hat{\bar{J}}_n{}^g$. The deviation in the vector potential due to discrete spatial effects, denoted as $\hat{\bar{\beta}}_n{}^g$, is obtained by evaluating the response of the plasma to the perturbation current $\hat{\bar{J}}_n{}^g$,

$$\hat{\bar{\beta}}_n{}^g = \frac{4\pi}{k^2 c} \hat{\bar{J}}_n{}^g(\omega)/D(k, \omega) \tag{C8}$$

where $k = 2\pi n/L$ and the dielectric function $D(k, \omega)$ may be written as

$$D(k, \omega) = 1 + (\omega_p{}^2/k^2c^2)[\omega/(\omega + \omega_c)].$$

Consider now the simulation of a whistler wave with a vector potential of the form $A(x, t) = \tilde{\beta}_n{}^w \exp[-i(kx - \omega_0 t)]$ for which $\hat{\bar{\beta}}_n = i\tilde{\beta}_n{}^w/(\omega + \omega_0)$ for $n = -kL/2\pi$ and $\hat{\bar{\beta}}_n = 0$ for $n \neq -kL/2\pi$. The dispersion function becomes

$$D = \omega_c(\omega + \omega_0)/[\omega_0(\omega + \omega_c)].$$

Substituting the proper terms from Eq. (C7) into Eq. (C8) and retaining only the second term in bracket in Eq. (C7) which is dominant yields

$$\frac{\hat{\tilde{\beta}}_n{}^g}{\tilde{\beta}_n{}^w} = \frac{4\pi^2}{L^2}\frac{\omega_p{}^2}{k^2c^2}\frac{v_{\perp 0}^2}{2}\frac{\omega_0(\omega+\omega_c)}{\omega_c(\omega+\omega_0)} \times \sum_{\substack{\sigma, \\ p\neq 0 \text{ or} \\ q\neq 0}} \frac{\bar{\psi}_{-n+pJ}\bar{\psi}_{n+qJ}n_\sigma}{(\omega+\omega_{(-n+pJ)\sigma}+\omega_c)^2(\omega+\omega_{(p+q)J\sigma}+\omega_0)} \tag{C9}$$

where $\bar{\psi}_n = Jn\bar{\varphi}_n$. Taking the inverse Laplace transform of Eq. (C9) gives discrete effect contributions from the single pole at $\omega = -\omega_0 - \omega_{(p+q)J\sigma}$ and the double-pole at $\omega = -\omega_c - \omega_{(-n+pJ)\sigma}$. Considering only the largest terms in the sum which correspond to $q = 0$ and $p = \pm 1$ yields Eqs. (23) and (24).

ACKNOWLEDGMENTS

Discussions of this paper with Professor O. Buneman are gratefully acknowledged.

This work is supported jointly by the U. S. Atomic Energy Commission under contract AT(11-1)-2200 and the Office of Naval Research under contract N00014-67-A-0356-0026. Acknowledgment is made to the National Center for Atmospheric Research, which is sponsored by the National Science Foundation, for computer time used in this research.

REFERENCES

1. R. N. SUDAN AND J. DENAVIT, *Physics Today* **26** (1973), 32.
2. J. DENAVIT AND R. N. SUDAN, to be published.
3. R. N. SUDAN, *Physics Fluids* **6** (1963), 57.
4. R. N. SUDAN AND E. OTT, *J. Geophys. Res.* **76** (1971), 4463.
5. A. BRUCE LANGDON, *J. Comput. Phys.* **6** (1970), 247.
6. C. G. DARWIN, Phil. Mag. **39** (1920), 537, see also J. D. JACKSON, "Classical Electrodynamics," pp. 409–411, Wiley, New York, 1962 or L. D. LANDAU AND E. M. LIFSHITZ, "Classical Theory of Fields," pp. 190–193, Addison–Wesley, Reading, Mass., 1962. The relativistic correction in the kinetic energy term has been neglected in Eq. (2).
7. A. N. KAUFMAN AND P. S. ROSTLER, *Physics Fluids* **14** (1971), 446.
8. H. RALPH LEWIS, "Methods of Computational Physics," Vol. 9, p. 307, Academic Press, New York, 1970.
9. Alternatively, the external field $\mathbf{B}_0$ may be included into the Lagrangian by adding an external vector potential $\mathbf{A}_0(y_i) = \mathbf{B}_0 y_i \hat{\mathbf{z}}$ to the internal potential $\mathbf{A}(x_i)$. The coordinates y_i drop out when writing the Euler–Lagrange equations and the formulation remains one-dimensional.
10. I. HABER, C. E. WAGNER, J. P. BORIS, AND J. M. DAWSON, "Proceedings of the Fourth Conference on Numerical Simulation of Plasmas," Naval Research Laboratory, Washington, D. C. (1970), 126.

11. J. DENAVIT, *J. Comp. Phys.* **9** (1972), 75.
12. W. P. GIBBONS, to be published. This algorithm was adapted from a band matrix solution, see for example D. H. THURNAU, Algorithm 195, CACM 8-63(441) and 12-72(1074), but allows for nonzero off-diagonal corner elements. The execution time is proportional to JM where J is the rank and M the number of nonzero diagonals.
13. J. M. DAWSON, *Phys. Rev.* **118** (1960), 381.
14. B. D. FRIED AND S. D. CONTE, "The Plasma Dispersion Function," Academic Press, New York, 1961.
15. With $\Delta v_x = c/10$ (21 beams) the maximum growth rate estimates are $\beta_{\sigma=0} = 0.027\ \omega_p$ for $v_{th} = c/3$ and $\beta_{\sigma=0} = 0.019\ \omega_p$ for $v_{th} = c/4.5$.Since electrostatic interactions do not play a role in the whistler beaming instability, Eqs. (16)–(18) involve the constants ω_p and c only through the skin depth $\lambda_m = c/\omega_p$. Explicit reference to these constants may therefore be eliminated by measuring time in units of ω_c^{-1} and length in units of λ_m. However, the normalization based on ω_p and c has been retained because the code actually includes electrostatic as well as magnetic interactions and the simulations require specific values of the ratios ω_c/ω_p and $\lambda_D/\lambda_m = v_{th}/c$.
16. A. BRUCE LANGDON, *J. Comput. Phys.* **12** (1973), 247.
17. H. RALPH LEWIS, A. SYKES AND J. A. WESSON, *J. Comput. Phys.* **10** (1972), 85.
18. J. DENAVIT AND R. N. SUDAN, *Phys. Rev. Lett.* **28** (1972), 404.
19. P. M. MORSE AND H. FESHBACK, "Methods of Theoretical Physics," p. 1322, McGraw–Hill, New York, 1953.